JOURNAL OF SYNCHROTRON RADIATION
ISSN 1600-5775

Understanding the instrumental profile of synchrotron radiation X-ray powder diffraction beamlines

Luca Rebuffi,[a]* Manuel Sánchez del Río,[b] Edoardo Busetto[a] and Paolo Scardi[c]

[a]Elettra-Sincrotrone Trieste SCpA, Trieste, Italy, [b]European Synchrotron Radiation Facility, Grenoble, France, and [c]Università degli Studi di Trento, Mesiano, Trento, Italy. *Correspondence e-mail: luca.rebuffi@elettra.eu

Received 27 October 2016
Accepted 10 April 2017

Edited by G. E. Ice, Oak Ridge National Laboratory, USA

Keywords: ray-tracing; powder diffraction; instrumental profile function; simulation.

A Monte Carlo algorithm has been developed to calculate the instrumental profile function of a powder diffraction synchrotron beamline. Realistic models of all optical elements are implemented in a ray-tracing software. The proposed approach and the emerging paradigm have been investigated and verified for several existing X-ray powder diffraction beamlines. The results, which can be extended to further facilities, show a new and general way of assessing the contribution of instrumental broadening to synchrotron radiation data, based on *ab initio* simulations.

1. Introduction

Most techniques in synchrotron radiation experiments, involving either soft or hard X-rays, extract the physical information by measuring radiation scattering, in terms of an intensity signal *versus* photon energy, detection position or angle, *etc*. The measured signal contains information on the X-ray–specimen interaction, but is also influenced by the characteristics of the X-ray beam and by the instrumentation, which are far from being ideal. The source characteristics (flux, size and divergences) are fundamental for any optical system. For instance, the best performing and expensive beamline in a low-emittance storage ring would simply not work, or it would give poor results, if installed in a conventional X-ray source or older generation synchrotron. The optics used to prepare the beam (for monochromatization, collimation, focusing) are never perfect. For synchrotron radiation where reflection of X-rays only occurs at low glancing angles (below a few mrad) the quality of the mirrors in terms of figure shape and finish is fundamental to obtaining the desired results. The monochromator, usually the heart of a synchrotron beamline, selects a narrow energy bandwidth required for the experiment. Downstream of the sample, the detector characteristics and performances must be considered when analysing the results, as usually the experimental results must be corrected for these. In between sample and detector there are usually other elements, slits or analysers, also playing an important role. Many experimental techniques base their success on a data analysis where the experimental results are compared with a model including the physics of the scattering phenomenon (absorption, diffraction, *etc*.), as well as a model of the broadening of instrument and detector caused by their non-ideality. Most data analysis routines include an approximate broadening, *e.g. via* convolution with Gaussians of adjustable breadth, with the only constraint of keeping the effect within a 'reasonable' range of values. In many cases, it is

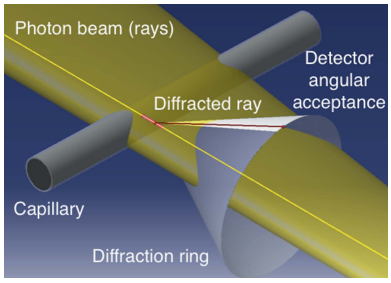

© 2017 International Union of Crystallography

possible to measure this instrumental broadening using a known, suitably characterized, reference sample.

Simulation tools in charge of modelling the beamline source and optics usually stop at the sample, providing information on beam size, divergence, energy spread and sometimes also polarization or coherence. Data analysis often starts with a good description of the sample, whereas the X-ray beam is less characterized. In the present work we try to bridge these two worlds, create a communication channel connecting an accurate and detailed simulation of the beamline optics with the sample's features, and describe how all is affected by the beam characteristics. The new approach is applied to a popular technique, powder diffraction. The ultimate goal is to enable virtual experiments, where the simulation includes all stages from the production of the X-rays to the experimental results for a particular sample. We show here that this is possible not only for illustrating how a beamline works but also to obtain quantitative information on the instrumental functions, which could be used in data analysis.

2. The instrumental function in powder diffraction

X-ray powder diffraction (XRPD) is a technique commonly used to characterize the spatial arrangement of atoms in materials. It provides structural information that can be correlated to functional characteristics, so that it is essential for investigating materials properties.

XRPD line profile analysis (LPA) is the chief technique in the study of materials microstructure (Mittemeijer & Scardi, 2004; Scardi *et al.*, 2004). Peak profiles in the diffraction pattern are modified in shape, intensity and position by microstructural effects, like the shape and size distribution of the crystalline domains (aka crystallites), lattice distortions (microstrain) and, in general, disorder present in the system. Together with these physical sources, the observed profile contains the instrumental contribution, which is a combined effect of photon source energy, spatial and angular divergence distributions of the photon beam, modelled by the specific optical setup and the quality of its elements, and radiation–matter interaction (mostly for the absorption effect).

The diffraction line profile observed experimentally (h) can be conceived as a convolution of the individual profiles of the different sources of instrumental broadening (g) and structural line broadening (f), such as crystallite size and microstrain (Klug & Alexander, 1974; Mittemeijer & Welzel, 2013),

$$h(\varepsilon) = \int_{-\infty}^{+\infty} g(\eta) f(\varepsilon - \eta)\, \mathrm{d}\eta. \qquad (1)$$

When dealing with nanostructured material, crystalline domain size produces significant effects on profiles. This can be treated according to Scherrer's formula (Scherrer, 1918; Patterson, 1939), correlating the measured integral breath β with the volume-weighted mean crystallite size $\langle D\rangle_{\mathrm{V}}$, incoming photon beam wavelength λ and diffraction angle θ,

$$\beta(2\theta) = \frac{K_\beta \lambda}{\langle D\rangle_{\mathrm{V}} \cos\theta}. \qquad (2)$$

Just by considering the inverse proportionality relation between the observed quantity and the mean crystallite size, it is clear how the error on the crystalline domain size diverges for small values of integral breadth, *i.e.* when instrumental effects are the main feature. Therefore, the LPA capability of determining the characteristics of materials, mostly with 'large' (several hundreds of nanometres) crystalline domains, is strongly affected by the shape and by the stability of the instrumental profile function (IPF). Studies based on such an 'at-the-limits' LPA are given by Malerba *et al.* (2014) and Fandaruff *et al.* (2015).

Synchrotron radiation seems the most appropriate choice to collect high-quality diffraction data, thanks to the high beam brilliance, energy selectivity and focusing conditions. But even a simple powder geometry can be affected by considerable aberrations (Gozzo *et al.*, 2010; Hinrichsen *et al.*, 2008), and the IPF needs to be 'well behaved', *i.e.* easily represented in convenient form for data analysis. This is particularly significant when dealing with the Debye scattering equation (DSE), which provides an expression for the diffraction from a randomly oriented powder of scatterers. Being based only on correlations between atom pairs (Debye, 1915; Warren, 1990), with no assumptions on crystalline structure and lattice defects, the DSE result is quite rigorous and general. Comparison with experimental data asks for diffraction patterns with small instrumental effects, in particular in terms of relative intensities and position of the peaks, *i.e.* small and well parameterized optical aberrations and negligible absorption effects.

Several mathematical descriptions of instrumental effects are available in the literature, in particular describing the optical origin of the diffracted beam divergence (Caglioti *et al.*, 1958; Sabine, 1987), and the optical aberration effects (Cheary & Coelho, 1998; Cheary *et al.*, 2004; Zuev, 2006, 2008). Corresponding expressions are used in data analysis methods like *TOPAS* (Cheary & Coelho, 1992) and whole powder pattern modelling (WPPM) (Scardi & Leoni, 2002; Scardi *et al.*, 2010) to build a parametric representation of the IPF, available for calibration and fitting procedures. In any case, the instrumental contribution to the diffraction pattern arises from the fact that neither the beam, nor the instrument, nor the sample are ideal. An ideal experiment has a strictly monochromatic and parallel X-ray beam delivered by an ideal monochromator, and analyses a point-like homogeneous specimen. The optical nature of the beamline elements naturally lends itself to a ray-tracing simulation approach for its description, prediction and analysis. Ray-tracing, in particular, seems appropriate to study the effect of the optics and to compute the IPF (Leoni *et al.*, 2004; Lambert & Guillet, 2008).

In real XRPD experiments the calculation of the IPF is typically obtained experimentally, by analysing the diffraction pattern of a standard reference material (SRM) like LaB_6 [NIST SRM 660 (Black *et al.*, 2010; Cline *et al.*, 2010)]. Since

this material gives narrow intrinsic peaks, the experimentally measured width is mainly due to instrumental effects.

In the WPPM approach (Scardi & Leoni, 2002; Scardi *et al.*, 2010), instrumental peak profiles are described by pseudo-Voigt curves, adopting a standard parameterization for the dependence of peak width and shape on the diffraction angle θ: Caglioti's equation is used for the full width at half-maximum (FWHM), whereas a parabolic function describes peak shape, in this case the Lorentz profile fraction η (aka pseudo-Voigt mixing parameter) (Caglioti *et al.*, 1958; Scardi *et al.*, 1994; Scardi & Leoni, 1999),

$$\mathrm{FWHM}(\theta) = \left[W + V\tan\theta + U\tan^2\theta\right]^{1/2}, \tag{3}$$

$$\eta(\theta) = a + b\theta + c\theta^2. \tag{4}$$

The apparent shift of the peak centroid $\Delta_{2\theta}(\theta)$, caused by aberrations along the beam path, is also parameterized using a $\tan\theta$ polynomial which closely follows Wilson's formulas (Wilson, 1963),

$$\Delta_{2\theta}(\theta) = ax\tan^{-1}\theta + bx + cx\tan\theta + dx\tan^2\theta + ex\tan^3\theta. \tag{5}$$

Parameters W, V, U, a, b, c, ax, bx, cx, dx, ex are adjusted to best fit experimental data collected for a sufficiently large number of peaks of the reference material across the whole accessible 2θ range. Additional aberrations, indirectly affecting the IPF, include a 2θ zero error and capillary alignment errors in horizontal and vertical directions (Cheary & Coelho, 1998; Cheary *et al.*, 2004). These parameters are used for describing the peak width and position shift as 2θ is scanned. They are quantitative but there is no direct physical meaning: one has to deduce them from fits and cannot anticipate *a priori* values knowing only the parameters influencing the photon beam characteristics.

3. Simulation of the scattering of rays by a powder sample in a capillary

We study here the possibility of creating a simulated instrumental profile by a Monte Carlo routine, to model the interaction of individual photons with a powder diffraction sample.

We represent the X-ray beam as a finite collection of rays, each one described by a starting position (s_x, s_y, s_z), direction (v_x, v_y, v_z) usually expressed through director cosines, and photon wavelength. Each ray has well defined parameters, therefore rays having different directions form a divergent beam, and rays with different photon wavelengths form a white beam. The ray wavevector is

$$\mathbf{k} = \frac{2\pi}{\lambda}\,\mathbf{v}. \tag{6}$$

The collection of rays describing the beam can be calculated using ray-tracing, given the characteristics of the source and a description of the optical elements. We adopted here the ray-tracing simulation software *SHADOW* (Sanchez del Rio *et al.*, 2011), where at the source the x axis is horizontal, z is vertical and y is directed along the main beam direction.

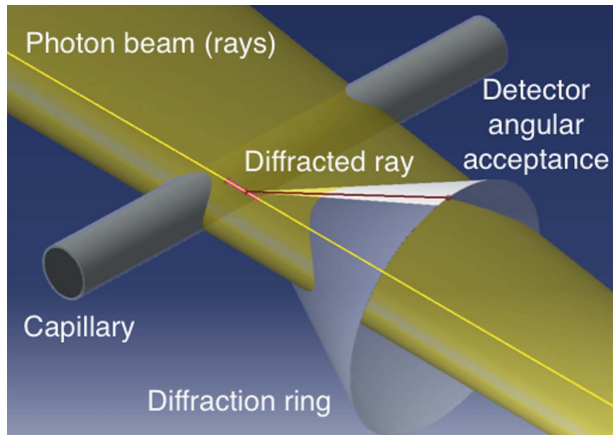

Figure 1
Geometry of the sample in a capillary glass. An incident ray (yellow) is diffracted by the powder sample inside the capillary. From all possible directions of the diffracted rays (a cone), an output diffraction range is chosen such that it will be accepted by detector or slit (area highlighted in white). Then a single diffracted ray (red) is chosen by Monte Carlo sampling.

The powder diffraction sample is considered to fill a glass capillary (see Fig. 1), as usual in synchrotron XRPD beamlines. The algorithm to model the sample should be able to generate a diffracted photon beam to be sent to the beamline simulator for further ray-tracing through the optical elements downstream of the sample, until the detector is reached. The final beam contains all the ingredients to display the XRPD pattern, from which one can calculate parameters like those of Caglioti's and Wilson's formulas [equations (3)–(5)].

3.1. Calculation of the diffraction direction

Ideally, for a given (h,k,l) reflection of an ideal sample (infinite number of randomly oriented crystallites, no microstructural effects and zero angular width for the intrinsic reflection), a ray-tracing algorithm for generating a diffracted beam of rays could rotate the wavevector of each incident ray by twice the angle obtained by using Bragg's law and the ray wavelength, around a rotation axis perpendicular to the incident ray direction. Such a model would create a Debye–Scherrer ring when considering all possible rotation axes perpendicular to the beam. In our case, we extended this idea to write the diffraction angle of each incident ray as

$$\theta^{hkl}_{\mathrm{diffracted}} = 2\left[\theta^{hkl}_{\mathrm{Bragg}}\left(\lambda_{\mathrm{ray}}\right) + \delta\theta_{\mathrm{Darwin}} + \delta\theta_{\mathrm{Size}}\right], \tag{7}$$

where $\theta^{hkl}_{\mathrm{Bragg}}$ verifies Bragg's law for the (h,k,l) reflection corresponding to the ray's wavelength,

$$\lambda_{\mathrm{ray}} = 2d_{hkl}\sin\theta^{hkl}_{\mathrm{Bragg}}. \tag{8}$$

The two corrections to Bragg's angle are:

(i) $\delta\theta_{\mathrm{Darwin}}$ accounting for the angular dispersion caused by the Darwin width $\Delta\theta_{\mathrm{Darwin}}$ of the sample material. The correction is approximated by adding an angle that follows a flat probability distribution in the range $[-\Delta\theta_{\mathrm{Darwin}}/2, \Delta\theta_{\mathrm{Darwin}}/2]$, according to a simplified diffraction

profile of the sample material, *i.e.* with no absorption and no tails (Zachariasen, 1945; Authier, 2001).

(ii) $\delta\theta_{\rm Size}$ accounting for the angular dispersion caused by the crystalline domain size distribution. It is assumed that size effects produce a Lorentzian profile, which is usually convoluted with other effects to obtain the diffraction profile (Mittemeijer & Welzel, 2008). The integral breadth $\beta(2\theta^{hkl}_{\rm Bragg})_{\rm Size}$ of the Lorentz distribution is calculated according to Scherrer's formula, as shown in equation (2), with $K_\beta = 4/3$ under the assumption of spherical crystallites.

Such a Lorentzian distribution (centered at $x = 0$) is given by

$$P(x) = \frac{1}{\pi\gamma\left[1 + (x/\gamma)^2\right]}, \tag{9}$$

with

$$\gamma = \frac{\rm FWHM}{2} = \frac{\beta\left(2\theta^{hkl}_{\rm Bragg}\right)_{\rm Size}}{\pi}. \tag{10}$$

This approximation is realistic for XRPD, accurate enough to take into account the small effects expected from a large-grained material like NIST SRMs, where the mean crystalline domain size is of the order of micrometers.

The scattering of each individual incident ray is thus generated by a rotation of its wavevector. The coordinates of the point where diffraction takes place are sitting along the ray trajectory, and are limited by the capillary volume. The particular position inside the capillary is randomly generated and depends on the capillary size and sample absorption, as will be discussed later. At this interaction point, the ray wavevector is rotated by the scattering angle [equation (7)] around a rotation axis versor $\mathbf{X}^{\rm rot}_{\rm ray}$. This rotation axis indeed depends on the particular ray as it must be perpendicular to its direction. It is calculated as

$$\mathbf{X}^{\rm rot}_{\rm ray} = \frac{\mathbf{k}}{|\mathbf{k}|} \times \left(\mathbf{X}_m \times \frac{\mathbf{k}}{|\mathbf{k}|}\right), \tag{11}$$

where $\mathbf{X}_m$ is the versor representing the X axis of the capillary system (which lies on the central symmetry axis of the capillary, positioned horizontally).

In order to reproduce the diffraction rings from a powder, the diffracted ray should be rotated around the wave versor $\mathbf{k}/|\mathbf{k}|$ by a random angle in $[0,2\pi]$. To prevent unnecessary loss of X-rays and make the simulation more efficient, this rotation angle is constrained to match the angular acceptance of the next optical system (a variance reduction technique), as illustrated in Fig. 1.

3.2. Calculation of the interaction point and inclusion of absorption effects

The simulation takes into account the absorption of the material, reducing the initial intensity I_0 of each incoming and diffracted ray according to the Beer–Lambert law,

$$I(\lambda, x) = I_0 \exp\left[-\mu(\lambda)\rho_{\rm eff}x\right], \tag{12}$$

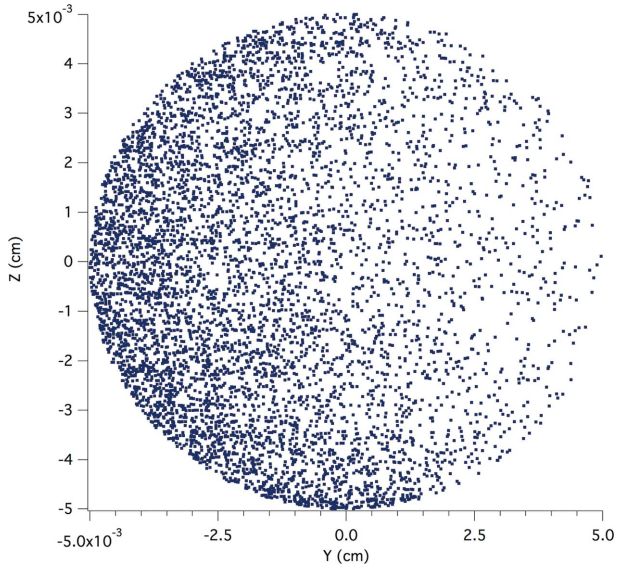

Figure 2
Cross section of a 0.1 mm-diameter capillary showing the points where the rays are diffracted. The distribution of the rays is due to the absorption of the material.

where $\mu(\lambda)$ is the linear absorption coefficient at the photon wavelength λ, $\rho_{\rm eff}$ is the material density multiplied by the packing factor of the sample into the capillary (typically around 0.6 for pure materials), and x is the path of the ray inside the capillary. The absorption effect is taken into account by calculating the starting point of the diffracted rays with a random generator based on an exponential probability distribution according to the transmitted intensity law [equation (12)].

This effect is important as the penetration of the rays inside the capillary is far from being uniform, so that a simpler flat distribution cannot correctly account for absorption in the ray-tracing procedure.

An example of the generated source points including X-ray absorption is shown in Fig. 2. Looking at the spatial distribution of the interaction points it is easy to figure out that the main effect of absorption is an apparent displacement of the capillary.

The absorption from the capillary walls has been taken into account and treated as well as the absorption of the sample material, with the possibility of a selection of materials: quartz glass, borosilicate glass and Kapton®. The attenuation coefficient in equation (12) requires knowledge of the material density, which is multiplied by the packing factor of the sample into the capillary (typically around 0.6 for pure materials).

3.3. Detector schemes and construction of the diffraction profile

Three experimental layouts have so far been implemented: (i) one-dimensional detector with collimating slits system, (ii) one-dimensional detector with an analyser crystal, (iii) two-dimensional detector. The experimental diffraction pattern of both one-dimensional detector systems is typically collected by a stepped rotation of the detector around the central

symmetry axis of the capillary, while collecting the diffracted signal for a fixed amount of time at every step (2θ angle scan): this procedure is simulated by repeating a ray-tracing of the capillary-to-detector optical system, incrementing a rotation angle (again, 2θ) of the system around the X axis of the capillary system of reference (central symmetry axis), by the same angular step. The experimental diffraction pattern of the two-dimensional detector system is obtained by ray-tracing the whole diffracted beam to a flat screen representing the active area of the detector, and then azimuthally integrating the obtained diffraction rings. Each diffraction peak height is normalized to the most intense one, calculated from the square modulus of the structure factor and the multiplicity of the reflection.

The final pattern is then obtained by introducing the Lorentz-polarization (LP) and thermal (T) factors, using the following expressions (Azároff, 1955; Yinghua, 1987; Lippmann & Schneider, 2000; Von Dreele & Rodriguez-Carvajal, 2008),

$$\mathrm{LP}(2\theta) = \begin{cases} \dfrac{1}{\sin\theta\sin\theta_{\mathrm{bragg}}}\dfrac{(1+Q)+(1-Q)\cos^2 2\theta\cos^2 2\theta_{\mathrm{mon}}}{1+\cos^2 2\theta_{\mathrm{mon}}} & \text{system of slits /area detector,} \\ \dfrac{1}{\sin\theta\sin\theta_{\mathrm{bragg}}}\dfrac{1+\cos^2 2\theta\cos^2 2\theta_{\mathrm{mon}}}{2} & \text{analyzer crystal,} \end{cases} \tag{13}$$

$$\mathrm{T}(2\theta) = \exp\left[-2B\left(\frac{\sin\theta}{\lambda}\right)^2\right], \tag{14}$$

where θ_{bragg} is the nominal Bragg angle of the reflection, Q is the degree of polarization (we used an approximate value of 0.95 for synchrotron radiation), θ_{mon} is the angle between the incident beam and the first crystal of the monochromator, and T is the temperature factor that depends on B, the Debye–Waller coefficient (in the present work, for simplicity, we consider an average scalar B value).

A complete ray-tracing simulation representing a powder diffraction experiment is shown in Fig. 3. The experiment for characterizing the IPF used a 0.8 mm Kapton® capillary filled with NIST 660b LaB_6 (Cline *et al.*, 2010), and a photon beam energy of 30 keV. The software calculates the IPF and also Caglioti's and Wilson's parameters by fitting a pseudo-Voigt to each generated diffraction peak.

It is worth noting that, in addition to any source of aberrations coming from the layout, the setup and optical characteristics of the beamline, the ray-tracing model automatically takes into account the diffractometer, the geometrical shape of the sample as well as other sources of positional aberrations like:

(i) displacement of the capillary with respect to the goniometric centre;

(ii) misalignments of the θ and 2θ goniometers axes: different position of the goniometric centres and different axis orientation;

(iii) displacement with respect to the ideal optical path of the optical elements between sample and detector, and of the detector screen in the two-dimensional case;

(iv) simple model of capillary wobbling, corresponding to a percent increase in diameter.

Sample and/or detection system misalignments are important issues in the XRPD practice. To cite just a few examples, displacement of the sample with respect to the ideal position shifts peak positions and makes peak shape asymmetric (Gozzo *et al.*, 2010); in two-dimensional detectors, tilt/tip of the screen produces an elliptical conic section with asymmetric thickness with respect to the tilt rotation axis; if not properly accounted for by a calibration procedure and treated by data reduction software, this aberration can generate artefacts in the resulting one-dimensional diffraction pattern (Cervellino *et al.*, 2006; Hart *et al.*, 2013).

The software also allows adding a background to the generated diffraction pattern, selecting and/or combining three different functions: constant value, Chebyshev polynomial (of the first kind up to sixth degree) and exponential decay. A random noise of adjustable intensity is added to the selected background curve.

Fig. 4(*a*) illustrates how the absorption calculation affects the peak intensities of the diffraction profile: by comparing the patterns with and without absorption calculation, normalized to the intensity of the most intense peak, the pattern with absorption shows an apparently smaller Debye–Waller coefficient with respect to the pattern without absorption. Another important effect of the absorption can be noticed in the peak shape, as visible in Fig. 4(*b*): with increasing values of μR (product of the linear absorption coefficient and the capillary radius), a progressive asymmetric shape appears, reducing the

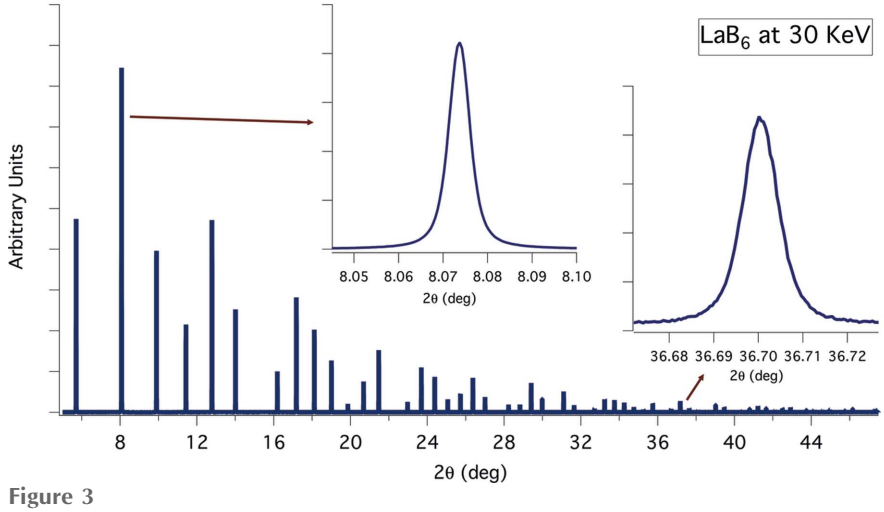

Figure 3
LaB_6 simulated diffraction pattern from a 0.8 mm capillary at 30 keV photon energy. Insets show details of the simulated peaks.

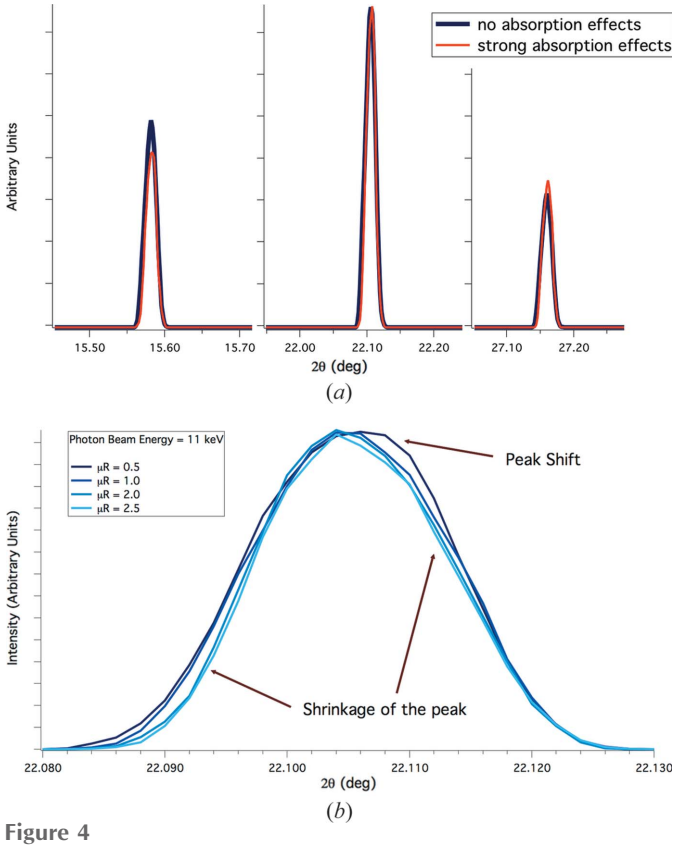

Figure 4
Comparison between simulated diffraction profiles of LaB_6 at 11 keV photon energy, with and without the absorption calculation: the first three peaks, normalized to the central one, are shown separately in (*a*). Effect of increasing absorption on the LaB_6 (110) peak at 11 keV: peak shape and position (*b*).

peak broadening, and shifting the peak. Peak position is crucial to accurately determine the cell parameters of the material; whereas instrumental shape and broadening affect the exact assessment of domain size and microstrain effects. The importance of keeping absorption under control (at least $\mu R \simeq 1$, but possibly well below unity) can then be understood, in order to maximize the precision and reliability of the LPA.

4. Understanding the IPF

4.1. Integration in the ray-tracing environment

The ray-tracing engine chosen for our simulations is *SHADOW3* (Sanchez del Rio *et al.*, 2011), embedded in its recently released user interface *ShadowOui* (Rebuffi & Sanchez del Rio, 2016). *ShadowOui* can selectively analyse the instrumental profile, studying the isolated effect of individual contributions (such as photon beam, or optical elements properties), and identify the most critical features affecting the final IPF.

A special *ShadowOui* element (called a widget, see Fig. 5) representing XRPD specimens (in capillary holder) simulating the interaction of the photons with matter was developed, with the target of analysing and predicting instrumental effects on experimental profiles (see Fig. 2). This widget drives the main

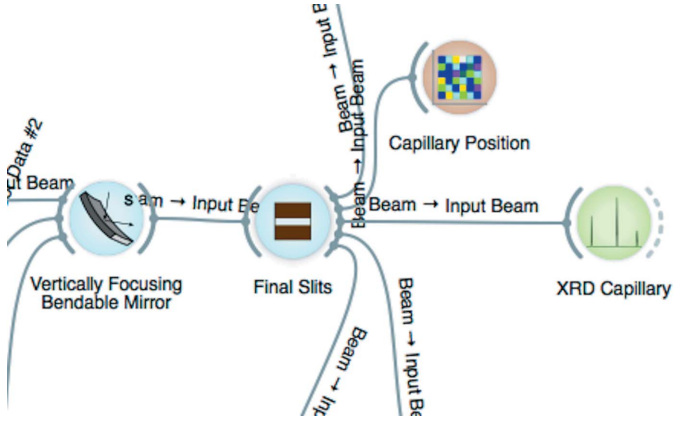

Figure 5
XRD widget in the *ShadowOui* graphic environment.

Python code implementing the algorithms described in the previous section.

The main crystal parameters such as Bragg angle and Darwin width, as well as photon–matter interaction cross sections including Rayleigh elastic scattering, Compton inelastic scattering and photoionization, are calculated by using the *xraylib* (Schoonjans *et al.*, 2011) routines.

The general principle is the simulation of the interaction between the photon beam generated by *SHADOW* and a capillary filled with a known crystal or standard, generating a diffracted photon beam and continuing the ray-tracing along the optical elements found in the beam path from specimen to detector. The incident beam is obtained by a ray-tracing simulation of the beamline with *ShadowOui*, using its capability of adding realistic features to the optical elements, like reflectivity (both for mirrors and crystals) and height error profile.

It is worth noting that, since our software is substantially a Monte Carlo ray-tracing procedure, it is not based on a concept of 'convergence' (like, for example, finite element analysis) but on the accumulation of a statistically significant amount of ray-tracing results, the meaning of which depends on the specific use. The computing time of a single bunch of rays depends on several aspects, primarily on the geometry of the sample (number of intercepted rays), and of the detection system, both of them again strongly dependent on the user's choice and on how the system has been designed. In other words, computation time is not directly predictable and is undefined within our software: the user is free to complete the simulation in less than one minute or to accumulate results for days.

4.2. Parametric assessment of the IPF

To properly assess the parameters influencing beam properties, and to independently study single contributions to the IPF, we separate the contribution of (i) photon source dimension, (ii) beam angular divergence and (iii) beam energy bandwidth. For this we simulated the photon source as purely geometrical with the different parameters relative to the three different studies reported in Table 1. We focused our attention

Table 1
Parameters of the source relative to the three studies of single IPF components.

Source dimension study	Angular divergence study	Energy bandwidth study
(i) Strictly monochromatic source (one emission line) (ii) Gaussian vertical and spatial shape parameterized by their vertical and horizontal σ (1, 10, 100 μm) (iii) Strictly parallel beam (no vertical or horizontal angular divergence)	(i) Strictly monochromatic source (one emission line) (ii) Point-like source (no spatial distribution) (iii) Uniform angular divergence distribution parameterized by their vertical and horizontal limit values (0.02, 0.2, 2.0 mrad)	(i) Uniform energy emission into a specified bandwidth (0.2, 0.8, 1.6, 3.2 eV) (ii) Point-like source (no spatial distribution) (iii) Strictly parallel beam (no vertical or horizontal angular divergence)

Table 2
Optical layout of MCX beamline at Elettra synchrotron.

Element	Description	Distance from source (m)
Storage ring	Energy = 2 GeV	
Source	Bending magnet (critical energy = 3.192 keV)	
Mask	Front-end angular acceptance: 2 mrad × 0.182 mrad	11.365
Mirror	Vertically collimating, Pt-coated, cylindrical mirror	15.400
Monochromator	Si(111) DCM, with sagittally bendable second crystal	18.000
Mirror	Vertically focusing, Pt-coated, cylindrical mirror	21.000
Sample position	Spot size of 1.0 mm × 0.15 mm	36.000

on the instrumental peak broadening (FWHM), since it is the most relevant feature in LPA.

The chosen beamline layout is that of MCX, the powder diffraction beamline at Elettra-Sincrotrone Trieste (Rebuffi *et al.*, 2014), details of which are reported in Table 2.

This beamline focuses the beam in both horizontal and vertical planes, approximately with one-to-one magnification. In the vertical, the focusing is in two steps: (i) mirror 1 collimates the beam to impinge on the monochromator with a negligible divergence, while gaining in energy resolution and flux, (ii) mirror 2 refocuses the beam on the sample. In the horizontal, the focusing is made by sagittally bending the second monochromator crystal.

In this study, double-crystal monochromator (DCM) elements are simulated as perfect crystals, mirrors have no slope errors and the uniform reflectivity is set to 1. The experiments for characterizing the IPF were carried out using a 0.1 mm capillary filled with NIST SRM 660a LaB_6 (Cline *et al.*, 2000) and photon beam energy of 11 keV, 15 keV and 20 keV.

The results calculated at 11 keV are reported in Fig. 6, showing that the most important feature in the IPF of a XRPD beamline is the energy bandwidth of the incident beam hitting the sample. In other words, the quality of the crystals and the residual divergence of the beam hitting the DCM play a crucial role. A weaker contribution comes from the angular divergence of the source: its increasing values produce an increasing collimating mirror residual divergence, leading to a larger bandwidth coming out of the DCM. Even if the bandwidth dependence on the energy distribution is stronger than the spatial distribution, the two effects combine in a real beamline and both contribute to the final IPF.

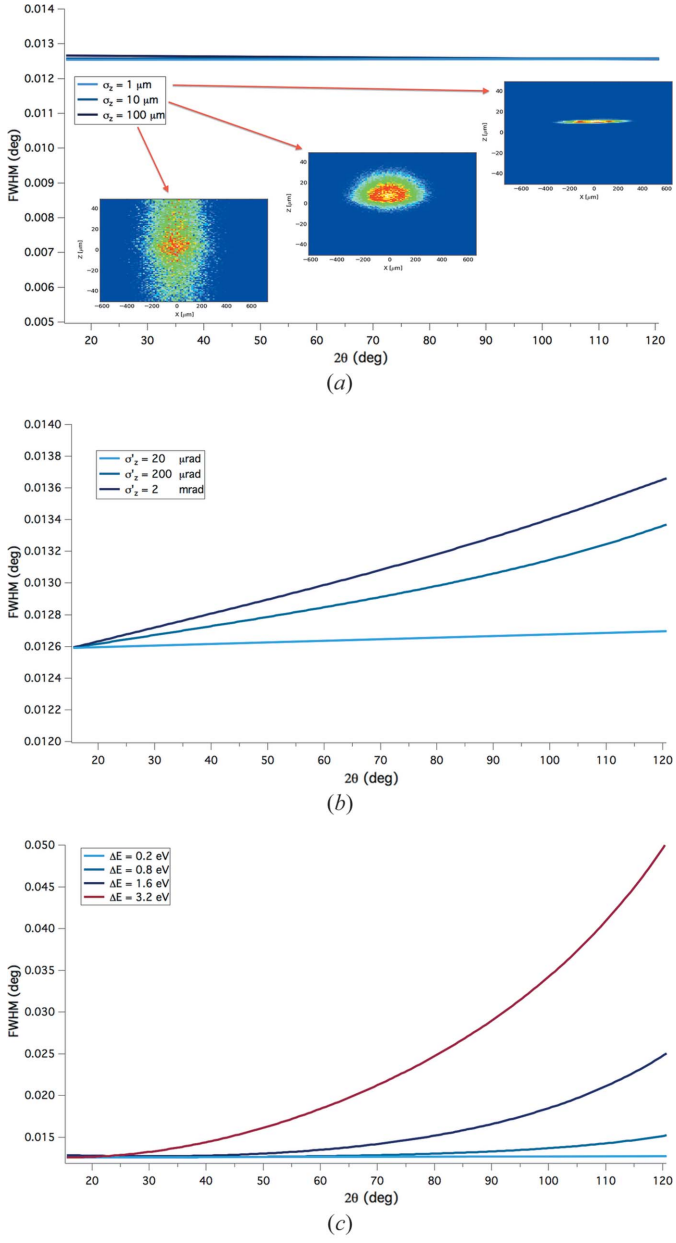

Figure 6
Effect of the source vertical dimension on the instrumental broadening at 11 keV; the insets represent the *XZ* projection of the beam (spot) at the quote of the origin of the capillary axis system. Similar results (not shown) are obtained with the horizontal dimension of the source. (*b*) Effect of the source vertical angular divergence on the instrumental broadening at 11 keV. (*c*) Effect of energy bandwidth on the instrumental broadening.

The source dimension plays practically no role for the values considered, confirming that the main factor in producing a minimum spot size at the detector (*i.e.* the minimum angular broadening, in the absence of any source of aberrations) is the diameter of the capillary: what the detection system actually sees is the source of the diffracted rays, the intersection of the beam with the capillary, and, in particular, the projection of this intersection on the horizontal plane under the angle of observation of the detector. From a purely geometrical optics point of view, diffraction from the capillary acts as a mirror at every Bragg's angle.

Without angular divergence and energy bandwidth, no dependence is produced in the instrumental broadening as a function of the 2θ angle. The results of the calculations made at 15 and 20 keV (not shown) are quite similar, confirming the conclusions of the previous analysis.

5. Comparison between simulated and measured IPF of existing beamlines

5.1. MCX at Elettra-Sincrotrone Trieste (1D detector with collimating slits system)

The simulation of the MCX beamline within the *ShadowOui* (Rebuffi & Sanchez del Rio, 2016) environment started with a careful optimization of the optical setup, in order to reproduce the experimental conditions as closely as possible:

(i) The source was simulated using the parameters of the MCX bending magnet.

(ii) Both mirrors include a height error profile: the first mirror is affected by the measured profile, available from the DABAM metrology database (Sanchez del Rio *et al.*, 2016), that can be retrieved and manipulated by the DABAM widget in *ShadowOui*; the second mirror uses a simulated height error profile with an average slope error equal to the measured one ($\sim$1.0 µrad).

(iii) Both mirrors include a platinum coating reflectivity. The material file is generated by a dedicated tool (PreRefl widget) in *ShadowOui*.

(iv) The diffraction profiles of the DCM crystals were generated for perfect crystals, again with a *ShadowOui* tool (Bragg widget). The second crystal of the DCM is cylindrically curved in the sagittal plane.

(v) Several sets of slits distributed along the beamline to properly shape the beam and limit the angular divergence were implemented in the simulations.

The simulated capillary was filled with a packing factor of 0.55, calculated by direct measurement of the transmittance at the beamline of the real capillary sample used for data collection for the SRM profile. Fig. 7 shows the *ShadowOui* representation of the whole beamline layout.

As discussed before, the energy bandwidth of the beam hitting the sample significantly affects the IPF, so it is important to analyse the DCM from a thermo-mechanical point of view. The first crystal is an ultra-high-quality flat single-crystal, with a measured Darwin width close to the theoretical value. This crystal is hit by the white beam, just collimated and filtered (to remove high energies) by the first mirror. The first crystal in the DCM absorbs nearly the full power of the beam, so its thermal load could be a possible source of deformation of the crystal planes, leading to unwanted effects of angular spreading of the beam, affecting the energy bandwidth, and

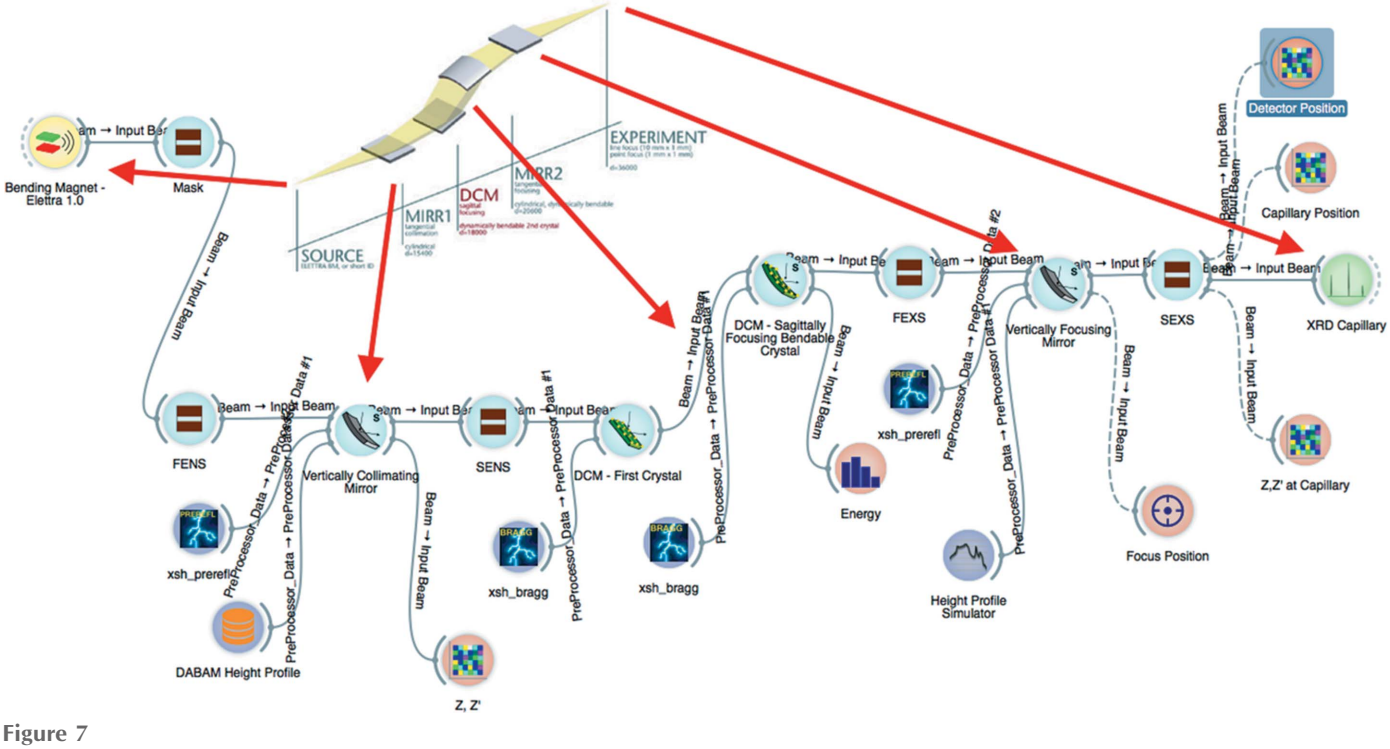

Figure 7
The MCX beamline layout represented as widgets in the *ShadowOui* canvas.

reducing the transmitted flux (Rutishauser *et al.*, 2013; Chumakov *et al.*, 2014). The case of MCX is not to be considered critical because the total power incident on the crystals, around 10 W in the worst situation (2 GeV storage ring energy and 310 mA of electron current), is easily dissipated by the water-cooling system.

The second crystal is mounted (soldered) on the ESRF model sagittal bender (Krisch *et al.*, 1991; Zhang *et al.*, 1998), a widely used stainless steel flexural hinge bender, shaping a near-cylindrical surface. Two motors, acting in opposite directions with identical force and pushing on the crystal holders, constitute the bending mechanism. This system is known to be a source of aberrations as it introduces anticlastic curvature in the crystal (for this the crystal is shaped with ribs in the back to minimize this effect) and twists the crystal as it bends. This is due to imperfections in the bending mechanism, and/or dimensional variations (Krisch *et al.*, 1991; Bilsborrow *et al.*, 2006), both producing not only a distortion in the shape of the beam but also a broadening of the bandwidth with respect to the ideal one.

It is worth noting that, in addition to the divergence of the beam coming out of the source, the collimating mirror contributes the global residual divergence of the outcoming beam for several reasons: (i) its height error profile, (ii) non-ideal near-elliptical shape, the curvature of which is obtained by a mechanical bending mechanism, (iii) thermal changes due to the illumination by the beam and gravity (Howell *et al.*, 2000). This residual divergence of the collimated beam incident on the DCM is also a source of broadening of the bandwidth.

In order to reproduce the experimental results from the real beamline, we combined several bandwidth broadening effects and optimized the simulation by: (i) broadening the Darwin widths by a factor of 1.1 for the first crystal and 2.0 for the second crystal, (ii) modifying the curvature of the first mirror in order to broaden the residual divergence from 15 µrad to 30 µrad.

The simulation was carried out at 15 keV, and results are reported in Fig. 8. As can be seen, a good agreement is obtained by introducing realistic features. The discrepancies between the experimental instrumental broadenings and the simulated ones, by using perfect crystal diffraction profiles and an ideally collimating mirror, confirm how critical a parameter is the bandwidth of the beam, as resulting from our IPF decomposition and analysis.

In order to check the goodness of the simulation from a purely optical point of view, we also compared the simulated spot at the sample with an image of the beam in the same position, as shown in Fig. 9: not only is the simulated beam section (1.58 mm × 0.30 mm) in good agreement with the real beam section (1.76 mm × 0.28 mm), but the introduction of a larger residual divergence generates a similar halo around the spot.

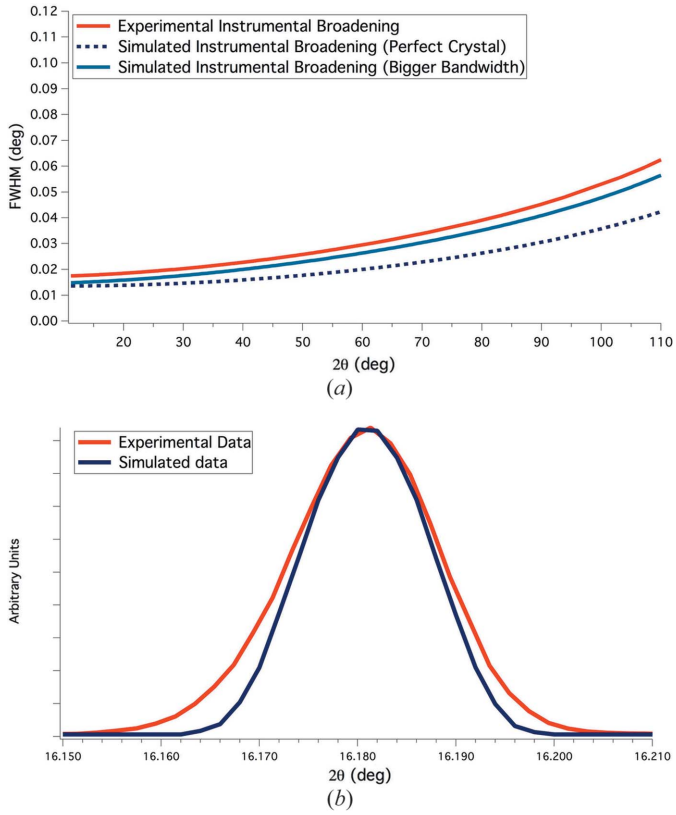

Figure 8
MCX beamline: comparison between experimental instrumental peak broadening and the simulated one, with theoretical diffraction profiles for the DCM crystals and perfect collimation (dotted blue line) and with diffraction profiles with larger Darwin width and a residual divergence on the collimating mirror (light blue full line) (*a*), together with a comparison between the experimental LaB_6 (110) peak and the simulated one (*b*). Central photon energy at the sample: 15 keV.

A further indirect verification of the goodness of the simulation came from the calculation of the flux at the sample, provided by the software *SPECTRA* (Tanaka, 2014, 2016). Calculation of the flux emerging from the source and our simulation to compute the beamline optical efficiency give 3.2×10^{10} photons s^{-1}, while a measurement of flux at the sample position with an ionization chamber gave a flux of $2.3\ (1) \times 10^{10}$ photons s^{-1}; the layout adopted to model the beamline and, in particular, the bandwidth seem therefore to be correctly reproduced.

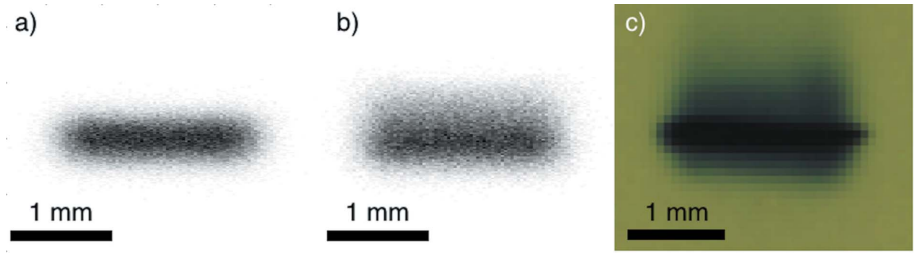

Figure 9
MCX beamline: comparison between simulated beam cross section at the sample: ideally collimating mirror (*a*), larger residual divergence (*b*), real spot image (*c*).

Table 3
Optical layout of 11-BM beamline at APS synchrotron.

Type	Description	Distance from source (m)
Storage ring	Energy = 7 GeV	
Source	Bending magnet (critical energy = 19.5 keV)	
Slits	White-beam slits	23.400
Mirror	Vertically collimating, Pt-coated, cylindrical mirror	26.000
Monochromator	Si(111) DCM, with sagittally bendable second crystal	27.600
Mirror	Vertically focusing, Pt-coated, cylindrical mirror	29.900
Sample position	Spot size of 1.5 mm × 0.5 mm	50.000

5.2. BM at APS (1D detector with analyser crystal)

We proceeded to check the reliability of our simulation tool by analysing a powder diffraction beamline with a detection system equipped with analyser crystals: the 11-BM beamline at APS (Wang *et al.*, 2008); its technical data are reported in Table 3.

The detector consists of 12 Si(111) analyser crystal/$LaCl_3$ scintillator detector optical systems, covering a total angular range of 24°. Each analyser crystal is mounted at a distance of 1 m, with entry slits of an adjustable aperture from 0.2 to 3 mm. The final signal emitted by the detector is actually similar to a convolution of the 12 separate signals (Lee *et al.*, 2008).

The experiment for characterizing the IPF used a 0.8 mm capillary filled with NIST SRM 660b LaB_6 (Cline *et al.*, 2010), and photon beam energy of 29.958 keV. Fig. 10 shows a comparison between experimental and simulated peak broadening [FWHM, (*a*)] and peak profile [(*b*)].

A good agreement is obtained by using the same configuration used for MCX in the simulation of the diffraction profile of the DCM crystals, which, as reported in the literature (Wang *et al.*, 2008), has a regular-shaped rocking curve under these operational conditions, but larger by a factor of about two.

It is worth noting that the experimental diffraction profile of LaB_6, when fitted by a pseudo-Voigt function, shows a predominant Lorentzian component (∼56%), which is not correctly reproduced by the simulation, having a predominantly Gaussian profile. This is clearly visible from a comparison of the tails of the diffraction peak in Fig. 10(*b*). A possible explanation considers that 11-BM is such a high-performing beamline in terms of low background and noise levels, high spatial resolution and narrow line profiles that we can presume it is able to detect even small effects coming from the SRM crystalline domains size distribution. In fact, according to the NIST certificate (Cline *et al.*, 2010), the measured particle size distribution of the powder accumulates 90% of the total amount of particles between 1 and 24 µm.

By considering that every particle is typically polycrystalline and thus composed of more than one crystalline domain, we can assume a mean crystalline domain size of the order of a few micrometers. In Fig. 11 it is possible to see a comparison

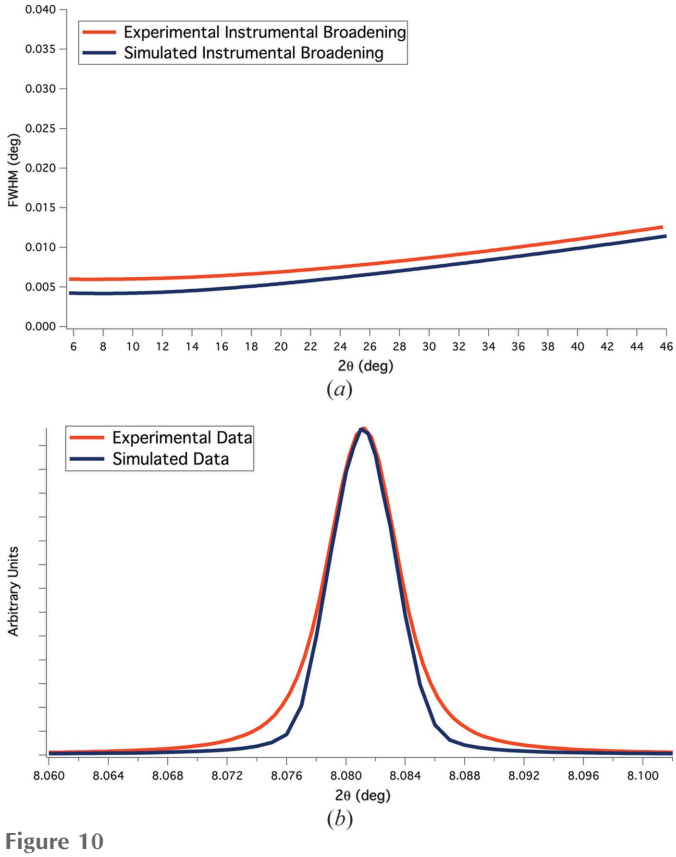

Figure 10
Comparison between experimental and simulated instrumental peak broadening (*a*), together with a comparison between the experimental LaB_6 (110) peak and simulated line profile (*b*). Central photon energy at the sample: 29.958 keV.

between the experimental diffraction profile of the LaB_6 (110) peak and the simulation, by specifying a progressively smaller mean crystalline domains size, and observing how the simulation is able to correctly reproduce the experimental profile with an optimized value of $\langle D \rangle_V$ = 2.8 µm. By using this value for the simulation of the IPF over the whole angular range, a significant improvement of the agreement with the experimental data is clearly visible in Fig. 12. By exporting this result

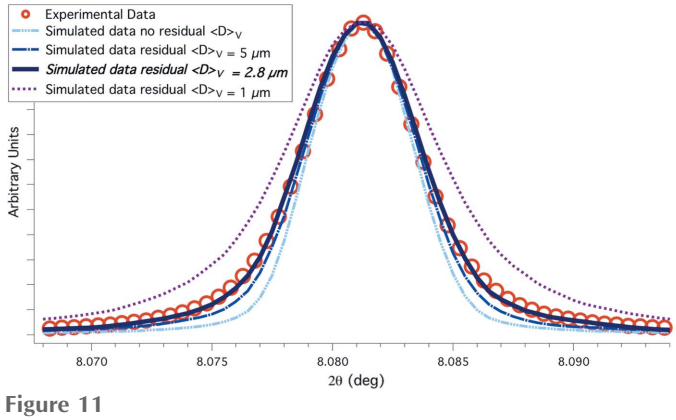

Figure 11
Comparison between the experimental LaB_6 (110) peak (red circles) and the simulated one, with progressively smaller mean crystalline domains size. The optimized value of $\langle D \rangle_V$ = 2.8 µm is represented by a full blue line.

Table 4
Optical layout of XRD1 beamline at Elettra synchrotron.

Type	Description	Distance from source (m)
Storage ring	Energy = 2 GeV	
Source	Hybrid multipole wiggler (Bernstorff *et al.*, 1995)	
Mask	Front-end angular acceptance: 1.5 mrad × 0.182 mrad	10.000
Mirror	Vertically collimating, Pt-coated, cylindrical (tangentially bendable) mirror	22.300
Monochromator	Nitrogen-cooled Si(111) double-crystal monochromator	24.500
Mirror	Vertically and horizontally focusing, Pt-coated, toroidal (tangentially bendable) mirror	28.000
Slits 1	Vertical and horizontal slits	37.800
Slits 2	Vertical and horizontal slits	38.700
Sample position	Spot size of 0.7 mm × 0.2 mm	41.000

to the MCX beamline simulation, we can observe similar remarkable effects on the profile, as visible in Fig. 13.

An important remark needs to be made with regard to the correct reproduction of the absorption effects, shown by the peak comparison in Fig. 13(*b*). The simulation, now improved to include the residual size effect of the measured LaB_6 powder, correctly reproduces the experimentally observed peak asymmetry.

5.3. XRD1 at Elettra-Sincrotrone Trieste (2D detector)

Finally, to test the last available detector configuration, we performed the simulation of a protein crystallography beamline equipped with an area detector, XRD1 at Elettra-Sincrotrone Trieste (Polentarutti, 2016). Technical details are reported in Table 4.

The XRD1 beamline is equipped with a Dectris Pilatus 2M area detector (Kraft *et al.*, 2009), which can be positioned at a variable distance in the range 85–1000 mm. The Pilatus 2M detector covers an active area of 254 mm × 289 mm, with a pixel of size 172 µm × 172 µm.

The experiment for characterizing the IPF used a 0.3 mm capillary filled with NIST SRM 660a LaB_6 (Cline *et al.*, 2000), and photon beam energy of 15 keV. Fig. 14 shows a comparison between experimental results and simulation, on the instrumental peak broadening (*a*), peak profile (*b*) and a comparison between the two-dimensional images from the Pilatus detector (*c*) and the simulated one (*d*).

Again a global good agreement is obtained, and the typical shape of the one-dimensional pattern coming from the integration of the rings of the two-dimensional image is correctly replicated; discrepancies between the experimental and simulated instrumental broadening appear for increasing scan angle, where the differences of the simulated crystal diffraction profiles and the real ones are more significant.

6. Quality evaluation: LPA with real and simulated IPFs

In order to check the quality of the simulation, a LPA with real samples was performed both with the measured IPF and with

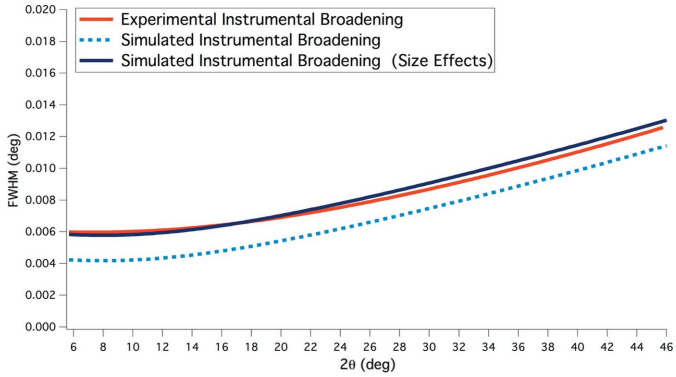

Figure 12
Comparison between the experimental diffraction profile at 15 keV central photon energy and the simulated one.

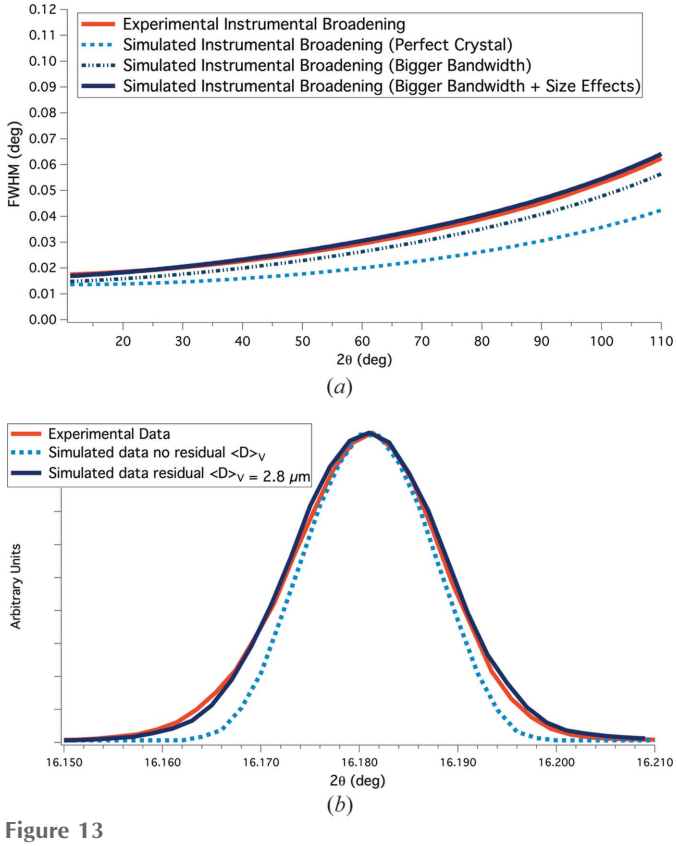

Figure 13
Comparison between the experimental instrumental peak broadening and the simulated ones at MCX beamline (*a*), together with a comparison between the experimental LaB_6 (110) peak and the simulated ones (*b*). Simulations were performed with mean crystalline domains size $\langle D \rangle_V$ = 2.8 µm (full blue line) and without size effects (dotted line). Central photon energy: 15 keV.

the simulated one. We used an XRPD profile measured at 15 keV at the MCX beamline, of an iron–molybdenum alloy powder (FeMo), that was extensively deformed by high-energy milling, so to refine the b.c.c. iron domain size to the nanometer scale (∼10 nm) and introduce a strong inhomogeneous strain. This profile was used in a detailed study on LPA reliability that can be found in the recent literature (Rebuffi & Río, 2016). FeMo data were analysed by WPPM,

using a well assessed procedure (D'Incau *et al.*, 2007): the equiaxed crystalline domains were described as a system of spheres with lognormally distributed diameters, containing straight dislocations of screw and edge type. Diffraction line profile components related to domain size/shape and to dislocations were convolved with the IPF to model the experimental data by non-linear least-squares minimization (Scardi, 2008; Scardi & Leoni, 2002). The free microstructural parameters in the refinement procedure were: lognormal mean (μ) and variance (σ) of the diameter distribution, average dislocation density (ρ) and effective outer cut-off radius (R_e). The anisotropic broadening effect of dislocations, according to the Krivoglaz–Wilkens theory (Krivoglaz & Ryaboshapka, 1963; Wilkens, 1970*a*,*b*), was described by an average contrast factor calculated for screw and edge dislocations in the primary slip system of b.c.c. iron 1/2(111){110} (D'Incau *et al.*, 2007). To account for the dislocation type, an edge/screw fraction parameter (f_E) was also refined. The comparison between results of WPPM is summarized in Table 5.

Table 5
WPPM results with measured and simulated IPF.

s.d. = standard deviation.

	Parameter	WPPM with experimental IPF	WPPM with simulated IPF (ideal)	WPPM with simulated IPF (realistic)
Size	$\langle D \rangle$	9.3 (8) nm	8.5 (7) nm	9.3 (8) nm
	s.d.	5.9 (9) nm	5.4 (9) nm	5.9 (9) nm
Strain	ρ	4.5 (4) $\times 10^{16}$ m^{-2}	5.3 (4) $\times 10^{16}$ m^{-2}	4.5 (3) $\times 10^{16}$ m^{-2}
	R_e	4.3 (4) nm	3.8 (4) nm	4.3 (4) nm
	f_E	0.54 (3)	0.52 (3)	0.54 (3)

One can notice that, while the realistically simulated IPF produces no differences in the fit results, the ideally simulated IPF produces a smaller average crystalline domain size and a higher dislocation density. This can be explained by considering that the simulation underestimates instrumental broadening. In particular, at higher scattering angle, as discussed by Rebuffi & Río (2016), while the size effects are constant throughout the reciprocal space and calculation of the parameters is dominated by the main low Miller indices peaks

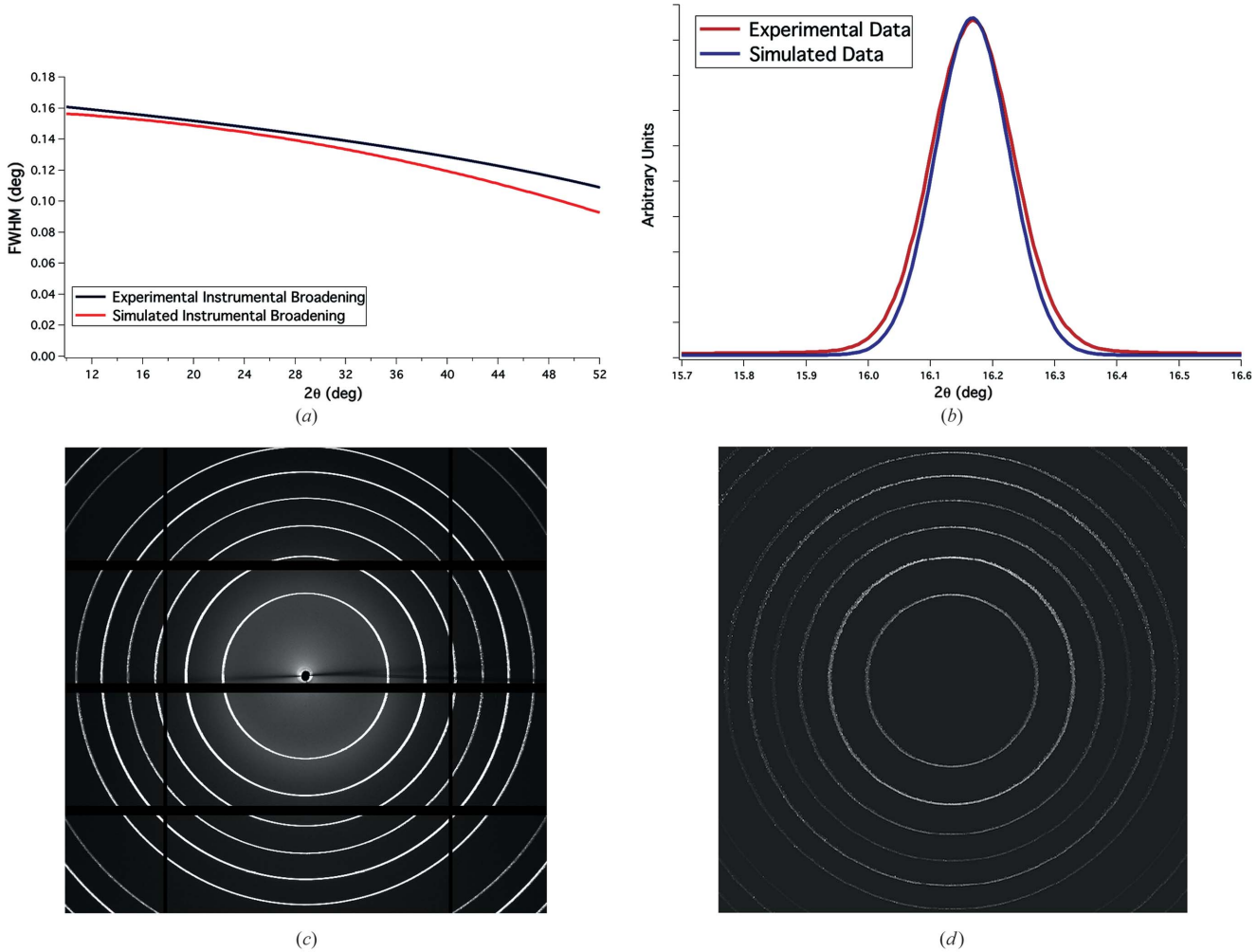

Figure 14
Comparison between experimental and simulated instrumental peak broadening (*a*) and LaB_6 (110) peak profile (*b*); Pilatus 2M two-dimensional image (*c*) and corresponding simulation (*d*). Central photon energy at the sample: 15 keV.

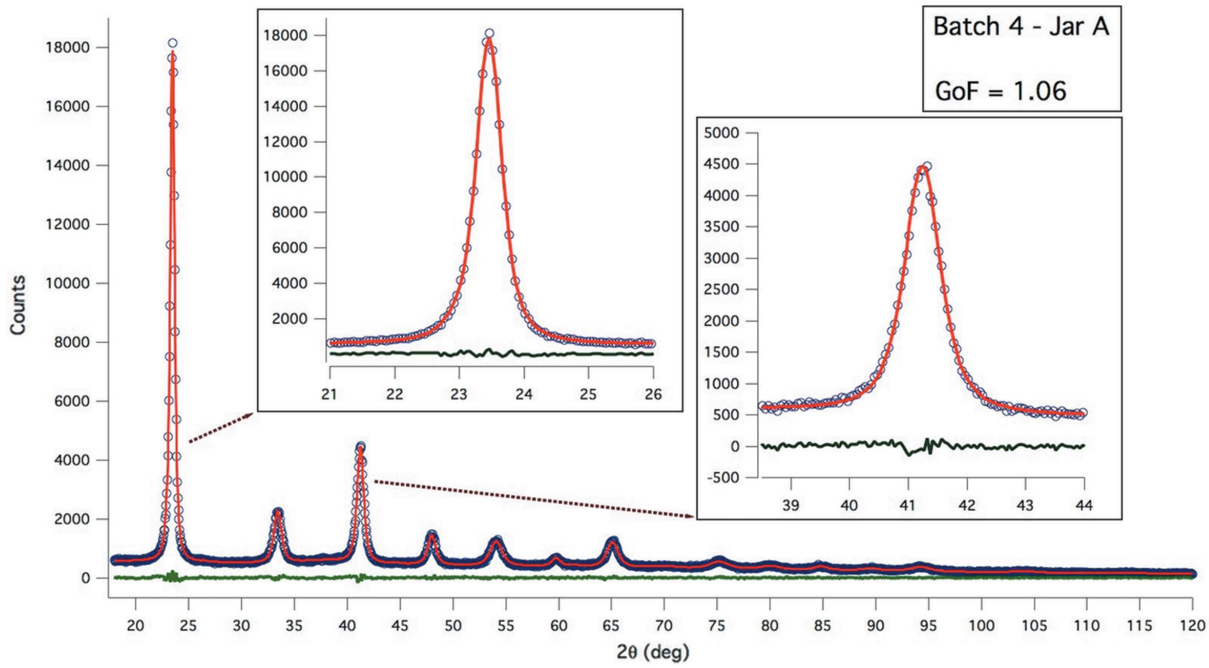

Figure 15
WPPM results with simulated IPF: MCX experimental data (circle), model (line) and residual (line below). Insets show details of the modelling of the two most intense reflections.

(where a better agreement between the experimental and simulated IPFs occurs), the broadening caused by strain increases with the angle, and the calculation of the fitted strain parameters is more sensitive to the fluctuations of the evaluated IPF. In Fig. 15 it is possible to see the WPPM fit with the simulated IPF in the 'ideal' configuration, observing the general accuracy of the result.

While a very good agreement with experimental data has been reached using deep knowledge of the beamline characteristics and performances, a good general agreement between the WPPM results with experimental and simulated IPFs has been obtained, indicating that the simulator gives reasonable data even if the real characteristics of the photon beam are not known, and 'tuning' of the simulation is not possible to the degree outlined in this work.

7. Summary and future work

A new algorithm for realistic ray-tracing of powder diffraction has been introduced. Given the results, it is a promising tool for simulating the instrumental effects in powder diffraction profiles at synchrotron radiation beamlines, and is fully integrated in the *ShadowOui* software environment.

As an off-line tool, it can be adopted by beamline users to drive experiment design and sample preparation, according to the beamline layout and beam energy. It also provides beamline scientists with the opportunity to improve the performance of existing beamlines. Finally, it can become a valid tool to improve the quality of design of optical components and beamline layouts, with a realistic experiment-oriented approach.

By analysing the case of XRPD, a comparison with experimental IPFs of three different beamlines, with different detection systems and at different energies, has been performed. Results show that the XRPD IPF is dominated by the energy distribution profile of the photon beam at the sample, which is principally determined by the crystals of the DCM.

In order to quantitatively check the quality of the simulated IPF, a comparison between LPA with WPPM on ball-milled iron–molybdenum alloy powder patterns using the experimentally measured instrumental broadening and the simulated one has been performed, obtaining compatible results. In a more general sense, the obtained results and the emerging paradigm of this work invite working on new IPF simulation widgets, dedicated to any other X-ray spectroscopy technique employed at synchrotron beamlines.

Future developments of this tool could introduce the XRD pattern dependence on sample pressure and temperature, which affect the resulting IPF when obtained by calibration with SRMs. Finally, the accurate calculation of the IPF could be the first step to simulating the diffraction pattern of a generic sample material, with its own (micro)structure and (micro)stress.

Acknowledgements

We want to warmly thank colleagues operating at the different beamlines, who really and kindly helped us a lot: Andrea Lausi and Jasper Plaisier from MCX at Elettra-Sincrotrone Trieste, Maurizio Polentarutti, Giorgio Bais and Nicola Demitri from XRD1 at Elettra-Sincrotrone Trieste, and, last but not least, Brian Toby from 11-BM at APS. Special thanks to Katia Casarin from the radioprotection group at Elettra-Sincrotrone Trieste for giving us a reliable measure of the flux at MCX beamline.

References

Authier, A. (2001). *Dynamical Theory of X-ray Diffraction, IUCr Monographs on Crystallography*, No. 11. Oxford University Press.
Azároff, L. V. (1955). *Acta Cryst.* **8**, 701–704.
Bernstorff, S., Busetto, E., Gramaccioni, C., Lausi, A., Olivi, L., Zanini, F., Savoia, A., Colapietro, M., Portalone, G., Camalli, M., Pifferi, A., Spagna, R., Barba, L. & Cassetta, A. (1995). *Rev. Sci. Instrum.* **66**, 1661–1664.
Bilsborrow, R. L., Atkinson, P. A., Bliss, N., Dent, A. J., Dobson, B. R. & Stephenson, P. C. (2006). *J. Synchrotron Rad.* **13**, 54–58.
Black, D. R., Windover, D., Henins, A., Filliben, J. & Cline, J. P. (2010). *Adv. X-ray Anal.* **54**, 140–148.
Caglioti, G., Paoletti, A. & Ricci, F. P. (1958). *Nucl. Instrum.* **3**, 223–228.
Cervellino, A., Giannini, C., Guagliardi, A. & Ladisa, M. (2006). *J. Appl. Cryst.* **39**, 745–748.
Cheary, R. W. & Coelho, A. (1992). *J. Appl. Cryst.* **25**, 109–121.
Cheary, R. W. & Coelho, A. A. (1998). *J. Appl. Cryst.* **31**, 862–868.
Cheary, R. W., Coelho, A. A. & Cline, J. P. (2004). *J. Res. Natl Inst. Stand. Technol.* **109**, 1–25.
Chumakov, A. I., Sergeev, I., Celse, J.-P., Rüffer, R., Lesourd, M., Zhang, L. & Sánchez del Río, M. (2014). *J. Synchrotron Rad.* **21**, 315–324.
Cline, J. P., Deslattes, R. D., Staudenmann, J.-L., Kessler, E. G., Hudson, L. T., Henins, A. & Cheary, R. W. (2000). SRM 660a. National Institute of Standards and Technology, Gaithersburg, MD, USA.
Cline, J. P., Deslattes, R. D., Staudenmann, J.-L., Kessler, E. G., Hudson, L. T., Henins, A. & Cheary, R. W. (2010). SRM 660b. National Institute of Standards and Technology, Gaithersburg, MD, USA.
Debye, P. J. W. (1915). *Ann. Phys.* **351**, 809–823.
D'Incau, M., Leoni, M. & Scardi, P. (2007). *J. Mater. Res.* **22**, 1744–1753.
Fandaruff, C., Segatto Silva, M. A., Galindo Bedor, D. C., de Santana, D. P., Rocha, H. V. A., Rebuffi, L., Azanza Ricardo, C. L., Scardi, P. & Cuffini, S. L. (2015). *Eur. J. Pharm. Biopharm.* **91**, 52–58.
Gozzo, F., Cervellino, A., Leoni, M., Scardi, P., Bergamaschi, A. & Schmitt, B. (2010). *Z. Kristallogr.* **225**, 616–624.
Hart, M. L., Drakopoulos, M., Reinhard, C. & Connolley, T. (2013). *J. Appl. Cryst.* **46**, 1249–1260.
Hinrichsen, B., Dinnebier, R. E. & Jansen, M. (2008). *Powder Diffraction: Theory and Practice*, edited by R. E. Dinnebier & S. J. L. Billinge, ch. 14, pp. 414–438. Cambridge: The Royal Society of Chemistry.
Howells, M. R., Cambie, D., Duarte, R. M., Irick, S., MacDowell, A. A., Padmore, H. A., Renner, T. R., Rah, S. & Sandler, R. (2000). *Opt. Eng.* **39**, 2748–2762.
Klug, H. P. & Alexander, L. E. (1974). *X-ray Diffraction Procedures*, 2nd ed. New York: John Wiley.
Kraft, P., Bergamaschi, A., Brönnimann, Ch., Dinapoli, R., Eikenberry, E. F., Graafsma, H., Henrich, B., Johnson, I., Kobas, M., Mozzanica, A., Schlepütz, C. M. & Schmitt, B. (2009). *IEEE Trans. Nucl. Sci.* **56**, 758–764.
Krisch, M., Freund, A., Marot, G. & Zhang, L. (1991). *Nucl. Instrum. Methods Phys. Res. A*, **305**, 208–213.
Krivoglaz, M. A. & Ryaboshapka, K. P. (1963). *Fiz. Met. Metalloved.* **15**, 18–31.
Lambert, S. & Guillet, F. (2008). *J. Appl. Cryst.* **41**, 153–160.
Lee, P. L., Shu, D., Ramanathan, M., Preissner, C., Wang, J., Beno, M. A., Von Dreele, R. B., Ribaud, L., Kurtz, C., Antao, S. M., Jiao, X. & Toby, B. H. (2008). *J. Synchrotron Rad.* **15**, 427–432.
Leoni, M., Welzel, U. & Scardi, P. (2004). *J. Res. Natl Inst. Stand. Technol.* **109**, 27–48.
Lippmann, T. & Schneider, J. R. (2000). *J. Appl. Cryst.* **33**, 156–167.
Malerba, C., Azanza Ricardo, C. L., Valentini, M., Biccari, F., Müller, M., Rebuffi, L., Esposito, E., Mangiapane, P., Scardi, P. & Mittiga, A. (2014). *J. Renew. Sustain. Energy*, **6**, 011404.
Mittemeijer, E. J. & Scardi, P. (2004). Editors. *Diffraction Analysis of the Microstructure of Materials*. Berlin: Springer.
Mittemeijer, E. J. & Welzel, U. (2013). *Modern Diffraction Methods*, edited by Eric J. Mittemeijer & Udo Welzel, pp. 89–126. Weiheim: Wiley-VCH.
Mittemeijer, E. J. & Welzel, U. (2008). *Z. Kristallogr.* **223**, 552–560.
Patterson, A. (1939). *Phys. Rev.* **56**, 978–982.
Polentarutti, M. (2016). *XRD1*, https://www.elettra.eu/elettra-beamlines/xrd1.html. Last accessed: 20 August 2016.
Rebuffi, L., Plaisier, J. R., Abdellatief, M., Lausi, A. & Scardi, P. (2014). *Z. Anorg. Allg. Chem.* **640**, 3100–3106.
Rebuffi, L. & Sánchez del Río, M. (2016). *J. Synchrotron Rad.* **23**, 1357–1367.
Rutishauser, S., Rack, A., Weitkamp, T., Kayser, Y., David, C. & Macrander, A. T. (2013). *J. Synchrotron Rad.* **20**, 300–305.
Sabine, T. M. (1987). *J. Appl. Cryst.* **20**, 173–178.
Sanchez del Rio, M., Bianchi, D., Cocco, D., Glass, M., Idir, M., Metz, J., Raimondi, L., Rebuffi, L., Reininger, R., Shi, X., Siewert, F., Spielmann-Jaeggi, S., Takacs, P., Tomasset, M., Tonnessen, T., Vivo, A. & Yashchuk, V. (2016). *J. Synchrotron Rad.* **23**, 665–678.
Sanchez del Rio, M., Canestrari, N., Jiang, F. & Cerrina, F. (2011). *J. Synchrotron Rad.* **18**, 708–716.
Scardi, P. (2008). *Powder Diffraction: Theory and Practice*, edited by R. E. Dinnebier & S. J. L. Billinge, Chapter 14, pp. 376–413. Cambridge: The Royal Society of Chemistry.
Scardi, P. & Leoni, M. (1999). *J. Appl. Cryst.* **32**, 671–682.
Scardi, P. & Leoni, M. (2002). *Acta Cryst.* A**58**, 190–200.
Scardi, P., Leoni, M. & Delhez, R. (2004). *J. Appl. Cryst.* **37**, 381–390.
Scardi, P., Lutterotti, L. & Maistrelli, P. (1994). *Powder Diffr.* **9**, 180–186.
Scardi, P., Ortolani, M. & Leoni, M. (2010). *Mater. Sci. Forum*, **651**, 155–171.
Scherrer, P. (1918). *Nachr. Ges. Wiss. Göttingen*, 26 September, pp. 98–100.
Schoonjans, T., Brunetti, A., Golosio, B., Sánchez del Río, M., Solé, V. A., Ferrero, C. & Vincze, L. (2011). *At. Spectrosc.* **66**, 776–784.
Tanaka, T. (2014). *Phys. Rev. ST-AB*, **17**, 060702.
Tanaka, T. (2016). *SPECTRA: a synchrotron radiation calculation code*, http://radiant.harima.riken.go.jp/spectra/.
Von Dreele, R. B. & Rodriguez-Carvajal, J. (2008). *Powder Diffraction: Theory and Practice*, ch. 3, pp. 58–88, edited by R. E. Dinnebier & S. J. L. Billinge. Cambridge: The Royal Society of Chemistry.
Wang, J., Toby, B. H., Lee, P. L., Ribaud, L., Antao, S. M., Kurtz, C., Ramanathan, M., Von Dreele, R. B. & Beno, M. A. (2008). *Rev. Sci. Instrum.* **79**, 085105.
Warren, B. E. (1990). *X-ray Diffraction.* New York: Dover.
Wilkens, M. (1970*a*). *Fundamental Aspects of Dislocation Theory*, Vol. II, pp. 1195–1221. Washington, DC: National Bureau of Standards.
Wilkens, M. (1970*b*). *Phys. Status Solidi A*, **2**, 359–370.
Wilson, A. J. C. (1963). *Mathematical Theory of X-ray Powder Diffractometry*. Eindhoven: Philips Technical Library.
Yinghua, W. (1987). *J. Appl. Cryst.* **20**, 258–259.
Zachariasen, W. H. (1945). *Theory of X-ray Diffraction in Crystals.* New York: John Wiley and Sons.
Zhang, L., Hustache, R., Hignette, O., Ziegler, E. & Freund, A. (1998). *J. Synchrotron Rad.* **5**, 804–807.
Zuev, A. D. (2006). *J. Appl. Cryst.* **39**, 304–314.
Zuev, A. D. (2008). *J. Appl. Cryst.* **41**, 115–123.